

Automatic Solar Flare Tracking Using Image Processing Techniques

Ming Qu and Frank Shih (shih@njit.edu)
College of Computing Sciences, New Jersey Institute of Technology
Newark, NJ 07102

Ju Jing and Haimin Wang
Center for Solar-Terrestrial Research, New Jersey Institute of Technology
Newark, NJ 07102
Big Bear Solar Observatory, New Jersey Institute of Technology
40386 North Shore Lane, Big Bear City, CA 92314

Feb. 9th, 2004

Abstract. Measurement of the evolution properties of solar flares through their complete cyclic development is crucial in the studies of Solar Physics. From the analysis of solar $H\alpha$ images, we used Support Vector Machines (SVMs) to automatically detect flares and applied image segmentation techniques to compute their properties. We also present a solution for automatically tracking the apparent separation motion of two-ribbon flares and measuring their moving direction and speed in the magnetic fields. From these measurements, with certain assumptions, we inferred the reconnection of the electric field as a measure of the rate of the magnetic reconnection in the corona. The automatic procedure is a valuable tool for real-time monitoring of flare evolution.

Keywords: Sun: activity - Sun: flares

1. Introduction

A solar flare is thought to be a result of an intense, abrupt release of solar magnetic energy by magnetic reconnection. A large number of high-energy electrons are accelerated, generating intense X-ray and radio bursts (Zirin, 1988). Plasma is heated to several million to tens of millions of degrees in the corona, emitting soft X-rays. Non-thermal electrons and thermal flux can rapidly heat the chromosphere causing it to emit in the $H\alpha$ wavelength. In an earlier paper we discussed the application of the Multi-Layer Perceptron (MLP), Radial Basis Function (RBF), and Support Vector Machine (SVM) to detect solar flares in real time (Qu et al., 2003). We have experimented and compared these three methods for solar flare detection using the solar $H\alpha$ images obtained at Big Bear Solar Observatory in California. In this paper we study the evolution of complex properties of the solar flares using image processing techniques and then propose a method for automatically tracking the ribbon separation motion of two-ribbon flares. The apparent motion of flare ribbons reflects the progress of magnetic reconnection. Measured properties of the flare evolution can be compared with associated



© 2004 Kluwer Academic Publishers. Printed in the Netherlands.

events such as coronal mass ejections (CMEs)(Yurchyshyn et al., 2000). The statistical analysis of flares must be derived by the studies of a large number of events, which can be achieved by an automatic detection program. This paper is organized as follows: Section 2 introduces the processes of automatic solar flare detection and characterization. Section 3 shows property measurement of solar flares using image segmentation techniques. Section 4 demonstrates automatic motion tracking of solar flares. Section 5 gives experimental results. Section 6 summarizes the conclusions.

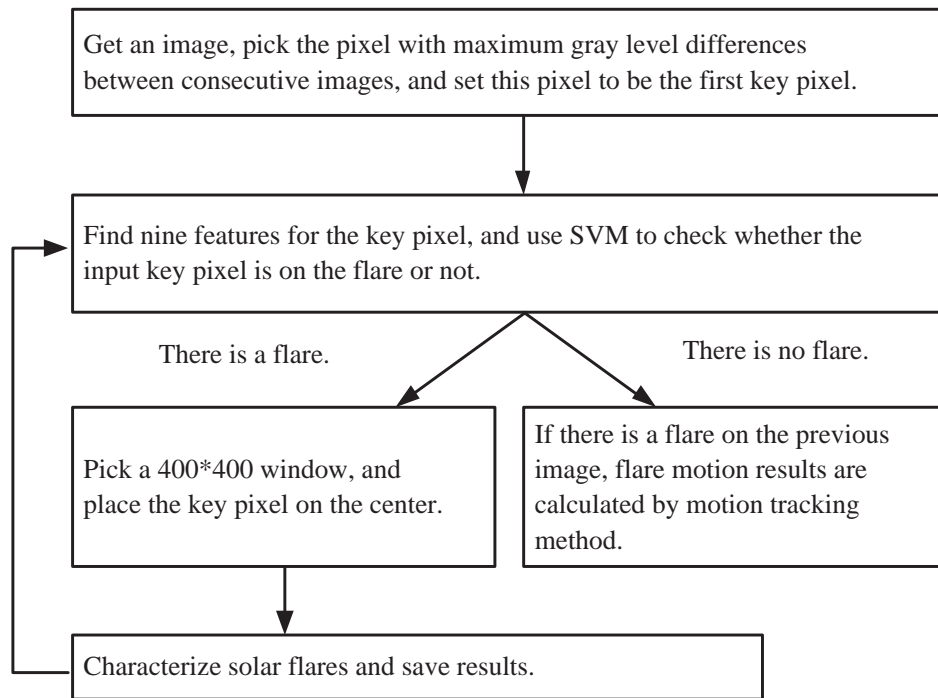
2. Solar Flare Detection And Characterization

2.1. SOLAR FLARE DETECTION

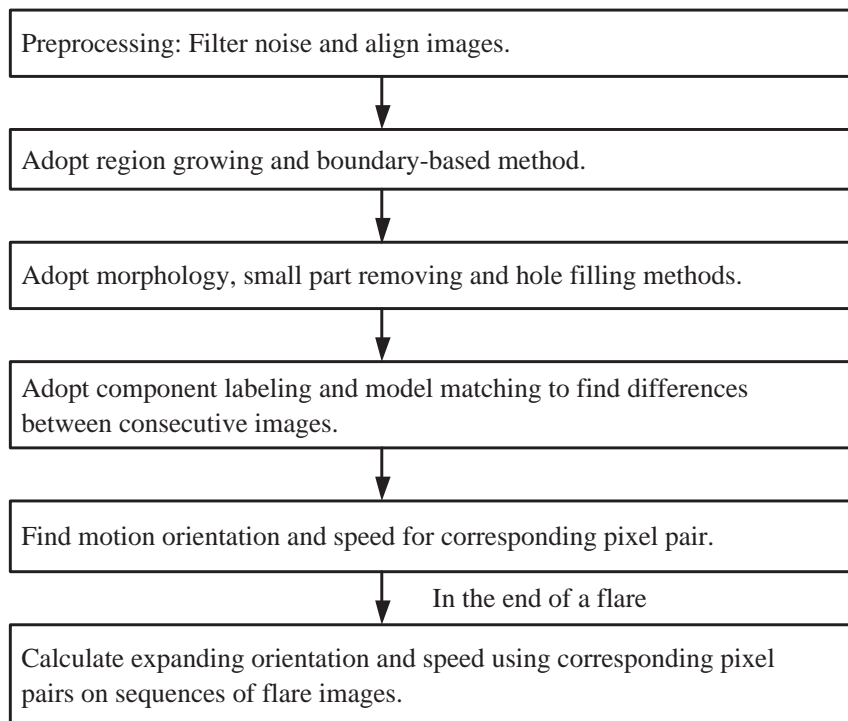
Automatic solar flare detection plays a key role in real-time space weather monitoring. In the previous paper RBF and SVM in addition to MLP were used to perform classification, and a set of nine features of solar images were developed as inputs (Qu et al., 2003). The classification is more than 95% successful and the running time is less than 0.3 second. When we focus on large flares, the classification rate is further improved. A key pixel is detected concurrently with a flare which has the maximum gray level difference between current and previous images. A solar image may have several key pixels when the image contains several flares. The position of a flare is obtained using the position of the key pixel , and the start time and end time of a flare are given by detecting a flare in a series of solar images. The diagram of the automatic solar flare detection is shown in Figure 1a.

2.2. AUTOMATIC SOLAR FLARE CHARACTERIZATION

The center of a solar flare is considered to be located at the key pixel. After detecting the position of a flare, we can measure the following properties: center position of a flare on the full-disk $H\alpha$ images, the number of pixels of a flare, lifetime of a flare tracked by comparing consecutive images, and the orientation and speed of a two-ribbon flare calculated by comparing differences between consecutive images. The first step of automatic characterization is preprocessing to filter noise and align the center of full disk solar images. Then the region growing, boundary-based detection, morphology, small part removing and hole filling method are used to obtain structure properties of a flare. Lastly motion of a two-ribbon flare is tracked by component labeling, model matching and pixel corresponding. The basic idea of pixel corresponding is that each pixel on the current model is correlated to a pixel on the previous model. Then the approximate motion of a two-ribbon flare is obtained by summarizing the motion of the corresponding pixels. The process is shown in Figure 1b.



(a)



(b)

Figure 1. a. Automatic procedure to detect and characterize flares. b. Automatic procedure to compute flare region and flare motion.

3. Solar Flare's Properties Measurement Using Image Segmentation Techniques

3.1. PREPROCESSING

In the preprocessing step image enhancement and filtering techniques were used to obtain high quality images. A median filter was used to remove additive noise and a recursive soft morphological filter is applied to be less sensitive to additive noise and small variations (Shih and Puttagunta, 1995). The center of the solar disk in each image was estimated to align images using their centers. A solar flare is a small feature on the full-disk solar image. In these experiments a 400×400 window was centered at the key pixel of a solar flare. The original gray level range of a solar image is between 0 and 32,767 and the mean brightness range of a 400×400 window is between 5,000 and 10,000. A good result was obtained when the mean brightness is around 8000. The following equation was used to normalize the mean brightness

$$x' = \frac{x \times 8000}{u} \quad (1)$$

where u denotes the mean brightness of the image, x is the original gray level, and x' is the resulting gray level.

3.2. REGION GROWING AND ADAPTIVE BOUNDARY-BASED METHOD

By combining both the region-based and adaptive boundary-based methods (Castleman, 1996), in addition to the morphological image processing techniques and hole filling techniques, the accurate boundary and the structure of flares is obtained. The region growing includes the bright part of a flare since the biggest part of a flare is the highly brightening area on the sun. The maximum gray level pixel in a 400×400 image is selected as the seed. The growing pixels have to be 8-connected to one of the pixels in seed regions and the neighbors' gray level must be greater than 80 percent of the seed. When a pixel satisfies the criteria, it is included in the seed region. The result of region growing is shown in Figure 2b.

The region-based method may lose detail near the edges of an object since it is hard to decide the threshold for region growing. Thus we adopt boundary-based methods such as the Sobel edge detector (Jähne, 1997) to enhance the boundary of a solar flare. In this experiment the first and second-order derivatives were considered for detecting the boundary of flares. The first-order derivatives are computed using gradient, and the second-order derivatives are obtained using Laplacian.

First-order derivatives of a digital image are based on various approximations of the 2-D gradient (Gonzalez and Woods, 2002). The gradient of

an image $f(x, y)$ is defined as a vector

$$\nabla \mathbf{f} = \begin{bmatrix} G_x \\ G_y \end{bmatrix} = \begin{bmatrix} \frac{\partial f}{\partial x} \\ \frac{\partial f}{\partial y} \end{bmatrix} \quad (2)$$

where G_x and G_y denote the gradients in x and y coordinates, respectively. Computation of the gradient is based on obtaining the partial derivatives at every pixel location. For a 3×3 area, Sobel operator is used to obtain G_x and G_y . The second-order derivative is defined as

$$\nabla^2 f = \frac{\partial^2 f}{\partial x^2} + \frac{\partial^2 f}{\partial y^2} \quad (3)$$

The edge of an object can be split into two sides: dark and bright. When a pixel is on the edge, $|\nabla \mathbf{f}| \geq T$, where T is a threshold; in addition, when a pixel is on the dark side, $\nabla^2 f \geq 0$, and on the bright side, $\nabla^2 f < 0$. The boundary is difficult to be detected using a single global threshold. An adaptive approach for handling such a situation is to divide the original image into sub-images and then utilize a different threshold for each sub-image. The 10×10 sub-image is adopted, and a threshold T is set according to the brightness and standard deviation of sub-images. The output of bright side pixels is assigned to 3, of dark side pixels to 2, and of background to 1. The results of the global and adaptive thresholding are shown respectively in Figures 2c and 2d. Note that for display purposes the values 1, 2, and 3 are mapped to gray levels 0, 128, and 255, respectively. A problem is observed from Figure 2d. The region enclosed by a small box has relatively low brightness compared to the flare region nearby. This region is not included since it is not inside the contour of the flare. However, when a higher threshold is used, some details of a flare maybe lost. Therefore we propose an improved method for adjustment in the following:

1. For each 10×10 sub-image, pick eight 10×10 windows of its neighbors.
2. Calculate its mean brightness and standard deviation.
3. Use the second largest mean brightness and standard deviation among all these windows as criteria for picking the threshold T .
4. When the mean brightness and standard deviation are large, use a large threshold; otherwise, a small threshold.

The result of the improved adaptive thresholding is shown in Figure 2e. The region growing method is used to expand the bright side area. The initial seeds for region growing are pixels on the bright side and the growing criterion is that the gray level is greater than or equal to the seed. Figure

2f shows the results. The result of the region growing is added to the result of the improved adaptive boundary method to have the best possible result as shown in Figure 2g.

3.3. MORPHOLOGY

Mathematical morphology, which is based on set-theoretical concept, can extract object features by choosing a suitable structuring shape as a probe. Two basic morphological operators are dilation and erosion. A binary image can be represented as a set, where "1" denotes the object pixel and "0" denotes the background pixel. Let A and B respectively denote the image and structuring element sets in Euclidean space. The reflection of set B , denoted \hat{B} , is defined as

$$\hat{B} = \{w | w = -b, \text{ for } b \in B\} \quad (4)$$

Both A and B as sets in X^2 , the dilation of A by B , denoted by $A \oplus B$, is defined as

$$A \oplus B = \{x | (\hat{B})_x \cap A \neq \emptyset\} \quad (5)$$

The erosion of A by B , denoted by $A \ominus B$, is defined as

$$A \ominus B = \{x | (B)_x \subseteq A\} \quad (6)$$

Dilation expands an image and erosion shrinks it. There are two other important morphological operators: opening and closing. Opening generally smooths the contour of an object, breaks narrow isthmuses and eliminates the protrusions. Closing tends to smooth sections of contours but, as opposed to opening, it generally fuses narrow breaks and long thin gulfs, eliminates small holes and fills gaps in the contour (Shih and Mitchell, 1989).

The opening of A by B , denoted by $A \circ B$, is defined as

$$A \circ B = (A \ominus B) \oplus B \quad (7)$$

Thus, the opening of A by B is the erosion of A by B , followed by the dilation of the result by B . Similarly, the closing of A by B , denoted by $A \bullet B$, is defined as

$$A \bullet B = (A \oplus B) \ominus B \quad (8)$$

The closing of A by B is simply the dilation of A by B , followed by the erosion of the result by B . The morphological closing is applied to the image in Figure 2g for erasing gaps and smoothing contours. The result is shown in Figure 2h, where a 3×3 structuring element with gray level of all ones is used.

3.4. SMALL PART REMOVING AND HOLE FILLING

In order to remove some small regions, the number of the pixels of each individual component in the binary image is counted. When the number of pixels in a component is less than a threshold, it is removed. To fill the small hole inside the flare, we propose a simple and efficient method. The segmented flare in the binary image is located at the bright region where the gray level is 1. A dark hole inside a flare is an individual dark region with a limited number of pixels. The number of pixels of each individual dark region is calculated. When the pixel number is less than a threshold, this dark hole is removed. The experiments show that a good threshold is 150.

Figure 2j shows the result of the small part removing and hole filling. Moreover we have proposed component labeling and model matching methods to extract regions of a flare. These methods are introduced in the following section because it is related to the motion tracking method.

4. Motion Tracking

In this section a standard method of manual measurement is reviewed and the new automatic measurement procedures for motion tracking are proposed.

4.1. STANDARD METHOD

As discussed in the introduction, the tracking ribbon separation speed is very important to understand the physics of magnetic reconnection for flares. In the previous work the motion of two-ribbon flares was not measured automatically (Qiu et al., 2003). First researchers outlined manually the trajectories of the flare ribbon fronts. Then the velocity of the ribbon expansion was determined as the time derivative of the distance between the successive trajectories. A running mean over several time frames was taken. The uncertainties generated by this method were discussed by Qiu et al. (2003). A major disadvantage is that the method is not entirely automatic.

4.2. COMPONENT LABELING AND MODEL MATCHING METHODS

There are two major techniques to estimate the motion in the field: differential techniques and matching techniques (Trucco and Verri, 1989). A solution is to build a flare model for an image and calculate differences between consecutive images using the previous segmented image results. For the first flare image, the component labeling technique is used to set the first three largest components as the main body of a flare and build

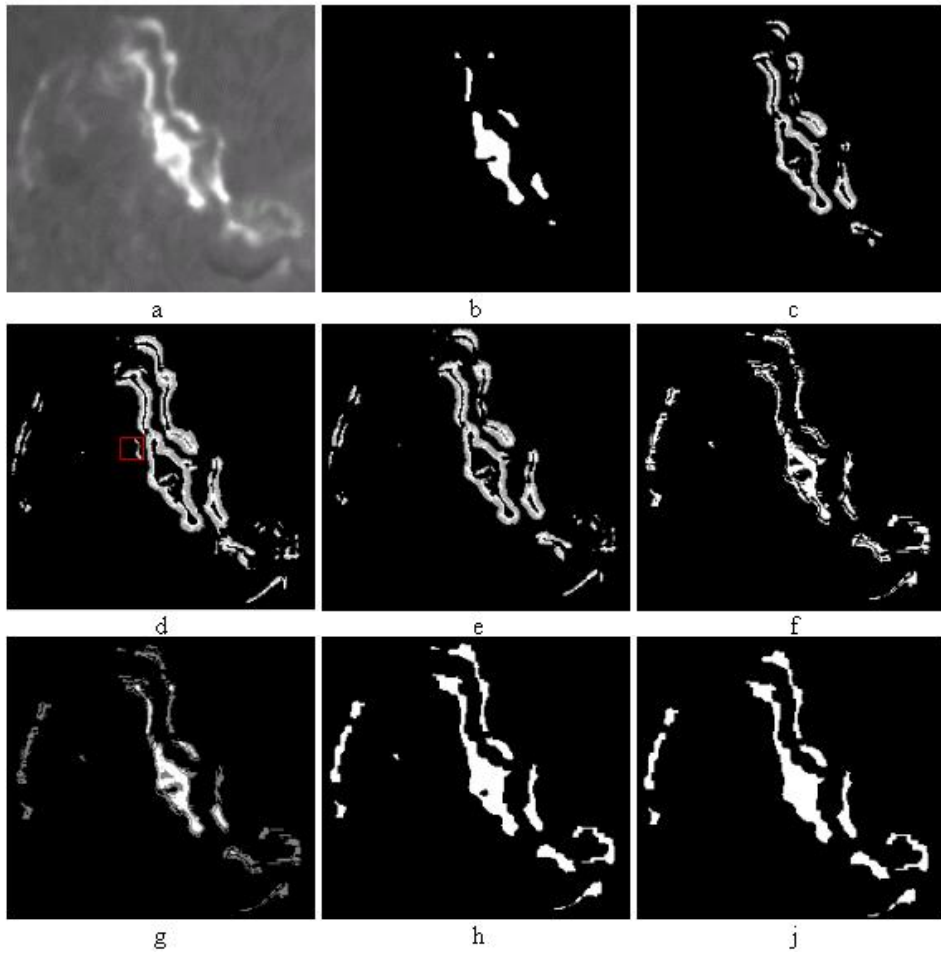


Figure 2. Image segmentation results for a flare peaked at 21:40:21 on 21 May 2002. a. Original image, b. result of the region growing, c. result of the global threshold boundary method, d. result of the adaptive threshold boundary method, e. result of the improved adaptive threshold method, f. result of the boundary growing method, g. result of the region growing plus result of the boundary growing method, h. result of the morphological closing, i. result of the small part removing and hole filling.

a model based on the component. Then the flare on the current image is matched with the previous model to obtain the flare components for the current image. To ensure the differences between consecutive images are selected, gray level differences on the original image are also taken into account. Thus a pixel pair is deleted from the result of differences when the pixel pair difference is very small.

To track the motion automatically, the same objects are labelled on consecutive images. For the first image, the smallest distance between regions

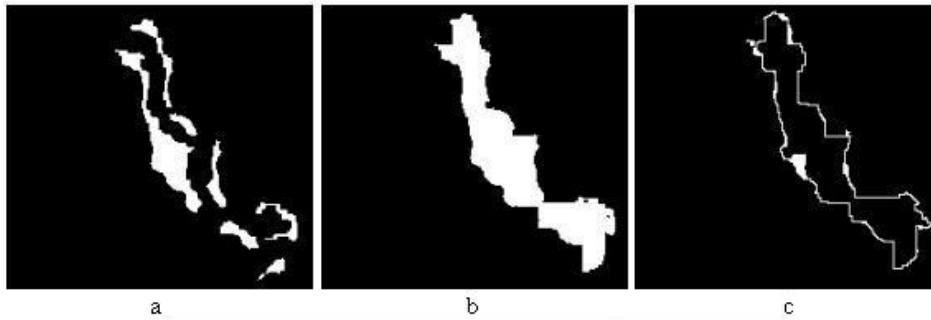


Figure 3. a.Result of the component labeling, b. result of the final model, c. result of the differences between the current and previous images.

is computed. When the smallest distance between two components is less than a threshold, they are merged; otherwise, they are labelled as different objects. The first three largest objects are selected to be the flare region. The result is shown in Figure 3a.

The separation of the two-ribbon flares can grow larger after certain time. It is no guarantee that these separated objects will be counted as the original flare using component labeling. Therefore we propose the following model matching method. A model is built for each image and match each object in the current image with the previous model. When an object overlaps with the previous image, this object is included to the current model. The model is created for the flare image as follows:

1. For the first image, use a morphological closing with a 15×15 structuring element to fill in the inside gap. For the images thereafter, use the previous model as the reference.
2. Obtain the differences between the segmented result and model result.
3. Remove the outer differences where the outer edge is recovered with the segmented result and keep the inner differences. Figure 3b demonstrates the result of the above three steps.

4.3. DIFFERENCE TRACKING AND PIXEL CORRESPONDING

Differences ($D1$) are obtained in Figure 3c using the current model minus the previous model. After having the current model, previous model, and differences between the current and previous models, the orientation and distance are measured for each pixel using the following method:

1. Let A = the edge of the current model, B = the edge of the previous model, and $C = 3A + 2B$. The pixels with gray level 5 are obtained on

C , where A and B are overlapped, $C = 3$ where the pixels are on the current model, and $C = 2$ where the pixels are on the previous model. The corresponding pixel ($C = 2$) on the previous model is correlated for each pixel ($C = 3$) on the current model. For instance, a nearest pixel (x_p, y_p) on the previous model can be found to correlate to a pixel (x_c, y_c) on the current model.

2. Obtain the orientation for each pair of corresponding pixels by

$$\theta_{c,p} = \arctan \left[\frac{y_c - y_p}{x_c - x_p} \right] \quad (9)$$

and the expansion distance by

$$d_{c,p} = \sqrt{(x_p - x_c)^2 + (y_p - y_c)^2} \quad (10)$$

Assign an increasing sequence number i to each flare image. For each flare image, record the number of pixels n and the mean of the expansion distance D on an approximate direction j , where $j = 1$ denotes the angle between $[-90^\circ, -80^\circ]$, $j = 2$ denotes between $[-80^\circ, -70^\circ]$, and so on.

$$D_{i,j} = \text{mean}(d_{c,p}) \quad (11)$$

where d is the resulting distance, i denotes the sequence number of a flare image, and j denotes the flare motion direction.

3. Calculate the two-ribbon flare motion using the pixels' motions. First estimate the approximate direction of the motion by checking the number of pixels in each orientation. Then compute the expansion speed s by

$$s_{i,j} = \frac{D_{i,j} - D_{(i-1),j}}{t} \quad (12)$$

where t denotes the time interval of consecutive images.

5. Experimental Results

The programs are developed in Interactive Data Language (IDL) by Research Systems, Inc. The programs run on a DELL Dimension L733r with CPU time 733 Mhz and memory of 256 Mbytes under Windows 2000. The process of image segmentation takes less than 20 seconds for each image, and the process of motion tracking takes less than 10 seconds. The computational time for the following processing steps is given in Table I: (1) image

Table I. Computational time (seconds) for each processing step.

Step	1	2	3	4	5	6
Time	3.9	6.2	0.8	4.7	6.3	1.8

preprocessing, (2) region growing and adaptive boundary processes, (3) morphological closing process, (4) small part removing and hole filling processes, (5) component labeling and model matching (6) pixel corresponding and motion tracking.

An H α two-ribbon flare event observed on May 21, 2002 from BBSO are selected to demonstrate the characterization results. In the following section the results of flare detection and characterization are demonstrated.

The starting and the ending time of a flare are obtained using the SVM classifier and an interval of two minutes is used to track speed. Component labeling and model matching are used to set the flare model. After building this model, outer difference pixels are obtained with consecutive models, and difference pixels are kept for each model. Each pixel on the current model corresponds to each pixel on the previous model for computing the orientation and speed of pixel's motion. The number of pixels and the median speed in each direction range are recorded. When a flare is over, the pixels are summed up to estimate the maximum number of pixels along a motion orientation. The speed for consecutive images is obtained using the pixel pairs' motion in this orientation. The results of component labeling, model matching and differences tracking are respectively shown in Figures 3a, 3b and 3c. The comparison of the two-ribbon flare's expansion distance between standard method and this automatic method is shown in Figure 4a. The results of the two methods are quite similar but the new results are obtained from automatic procedure.

The magnetic reconnection rate is measured in term of electric field E in reconnection current sheet. Methods and uncertainties of these measurements are extensively discussed by Qiu et al. (2003). Using the automatic method, the expansion velocity V_r of flare ribbons is computed and the ribbon with the magnetic fields B_n they sweep through is aligned. This method detects all the moving pixels and obtain accurate B_n by using the average B of moving pixels. E is obtained by

$$E = V_r \times B_n \quad (13)$$

The comparison of the E field between standard method and the automatic method is shown in Figure 4b. Compared with the previous method which tracks the moving front of ribbons manually, this method has the

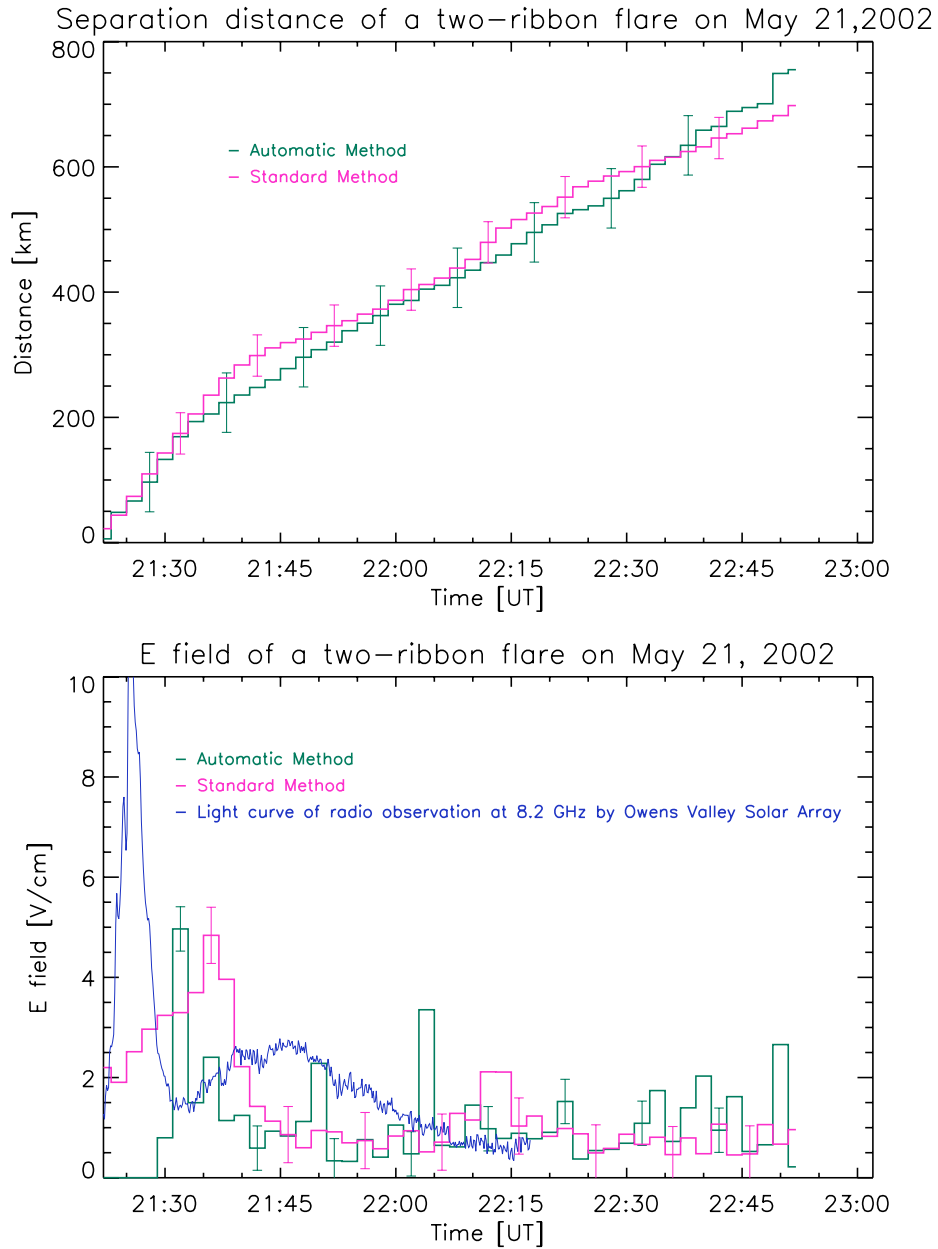


Figure 4. a. Comparison of the two-ribbon separation distance as a function of time for the flare happened on May 21, 2002. The red curve denotes the result of the standard method and the green curve denotes the result of the automatic method. b. Comparison of derived electric field of the two-ribbon flare. The light curve of 8.2 GHz radio emission is overlotted to indicate onset of the flare.

following advantages: 1) it avoids the difficulty in determining the positions of the moving front which usually do not have a regular and clear shape, and 2) an accurate average is obtained by considering all the B_n 's in the newly brightened area. However, the results of automatic method also contain errors due to noise effect. The confidence intervals of both methods are estimated by computing the standard deviation of parameters in the background level, which are shown in Figure 4 with error bars. In general, the deviations between two sets of results are acceptable. On the study of solar flares, scientists are most interested in the total separation distance shown in Figure 4a and the peak value of the electric field shown in Figure 4b. Figure 4b shows that the automatic method can obtain a better result than the standard method in Qiu et al. since the peak of the E field from the automatic result is closer to the peak of the light curve of the flare as observed in the radio.

6. Conclusions

In this paper automatic solar flare detection and characterization are presented. Region growing and boundary-based methods are combined to obtain the detailed properties of solar flares. The morphology technique, small part removing and hole filling are used to further improve the performance. Component labeling and model matching techniques are used to characterize the main region of a flare. We also propose a motion tracking method to compute the orientation and speed of two-ribbon flares automatically. The processes of image segmentation and motion tracking take less than 30 seconds for each image and the results are accurate. Moreover the E field of magnetic reconnection current sheet is obtained by this automatic program and verify the result of Qiu et al (2003). This automatic process is valuable for the forecasting and studies of solar flares since this process dramatically improves efficiency and accuracy. The method allows us to study the evolution of a large number of solar flares efficiently, which will help space weather forecasting.

Acknowledgements

We would like to thank Dr. Alex Young for many suggestions that greatly improved this paper. This work is supported by National Science Foundation (NSF) under grants IIS-0324816, ATM 0233931 and ATM 0313591.

References

- Castleman, K. R. *Digital Image Processing*. Prentice Hall, 1996.
- Gonzalez, R.C. and Woods, R.E. *Digital Image Processing*. Prentice Hall, 2002.
- Jähne, B. *Digital Image Processing*. Springer, 1997.
- Martin, S.F. Mass Motions Associated with Solar Flares. *Journal of Solar Physics*, 121, 215-238, 1989.
- Qu, M., Shih, F.Y., Jing, J., and Wang, H. Automatic Solar Flare Detection Using MLP, RBF and SVM. *Journal of Solar Physics*, 217, 157-172, 2003.
- Qiu, J., Wang, H., Cheng, C.Z., Gary, D.E. Magnetic Reconnection and Mass Acceleration in Flare - Coronal Mass Ejection Events. *Astrophysical Journal*, in press, 2003.
- Shih, F.Y. and Mitchell, O.R. Threshold Decomposition of Grayscale Morphology into Binary Morphology. *IEEE Trans. Pattern Analysis and Machine Intelligence*, v11, no. 1, 31-42, 1989.
- Shih, F.Y. and Puttagunta, P. Recursive Soft Morphological Filters. *IEEE Transactions on Image Processing*, v4., No. 7, 1027-1032, 1995.
- Trucco, E. and Verri, A. *Introductory Techniques for 3-D Computer Vision*. Prentice Hall, 1989.
- Yurchyshyn, V. B., Wang, H., Qiu, J., Goode, P. R. and Abramenko, V. I. Magnetic Topology in 1998 November 5 Two-Ribbon Flare as Inferred from Ground-based Observations and Linear Force-free Field Modeling. *Astrophysical Journal*, 540, 2000.
- Zirin, H. *Astrophysics of the Sun*. Cambridge University Press, Cambridge, 1988.